Order and chaos in the rotation and revolution of two massive line segments

Andrew Blaikie,[1] Alex D. Saines,[1] Matthew Schmitthenner,[1] Maggie Lankford,[1] R. Drew Pasteur,[2] and John F. Lindner[1]
[1]*Physics Department, The College of Wooster Wooster, Wooster, Ohio 44691, USA*
[2]*Mathematics and Computer Science Department, The College of Wooster, Wooster, Ohio 44691, USA*
(Received 11 October 2013; published 28 April 2014)

As a generalization of Newton's two body problem, we explore the dynamics of two massive line segments interacting gravitationally. The extension of each line segment or slash (/) provides extra degrees of freedom that enable the interplay between rotation and revolution in an especially simple example. This slash-slash (//) body problem can thereby elucidate the dynamics of nonspherical space structures, from asteroids to space stations. Fortunately, as we show, Newton's laws imply exact algebraic expressions for the force and torque between the slashes, and this greatly facilitates analysis. The diverse dynamics include a stable synchronous orbit, families of unstable periodic orbits, generic chaotic orbits, and spin-orbit coupling that can unbind the slashes. In particular, retrograde orbits where the slashes spin opposite to their orbits are stable, with regular dynamics and smooth parameter spaces, while prograde orbits are unstable, with chaotic dynamics and fractal parameter spaces.

DOI: 10.1103/PhysRevE.89.042917 PACS number(s): 05.45.−a, 95.10.Fh, 95.10.Ce, 45.50.Pk

I. INTRODUCTION

The dynamics of two point particles interacting gravitationally is one of the most famous problems in classical mechanics. The solution to this celestial two body or dot-dot (··) problem includes the beautiful result that all the orbits are conic sections. The two body solution explains Kepler's laws and anchors our understanding of the solar system. Newton's "superb theorem" [1], which states that spherically symmetric bodies gravitate as if all their masses are located at their centers, ensures the two body solution's practicality, as stars and planets are naturally nearly spherical.

It is reasonable to try to extend this success to nearby problems. However, the chaotic dynamics enabled by the addition of just one more particle both enriches and complicates such progress, prompting Newton to write, "My brain never hurt more than in my studies of the Moon (and Earth and Sun)" [2]. While the three and N body problems remain centrally important [3–6], extensions are possible in other directions. For example, contemporary variations of the two body problem can also exhibit chaotic dynamics. Confining two interacting bodies to a spherical universe results in arbitrarily complicated orbits due to the compactness of the space [7]. Preserving Newton's second law but inverting Newton's third law converts regular two body dynamics into chaotic dynamics [8]. Relaxing the point mass approximations leads to the full body problem [9], in which masses have arbitrary rotational inertias and experience net torques as well as net forces. Connecting two point masses by a massless rod [10] or a spring [11] can model artificial and tethered satellite systems or tidal synchronization and orbit circularization [12].

In 2000 and 2001, NASA's NEAR-Shoemaker spacecraft became the first to orbit and land on an asteroid, the potato-shaped 433 Eros [14]. In 2003, Elipe and Lara [15] studied the motion of a point particle orbiting a rotating line segment as a simple model of NEAR orbiting Eros. In 2010, Lindner *et al.* [16] considered more generally the dynamics of a massive line segment or slash (/) and a massive point or dot (·) interacting gravitationally. For this slash-dot (/.) body problem, they derived algebraic expressions for the force and torque on the slash and studied the flow of angular momentum from spin to orbit. The slash-dot body problem is a natural extension of the dot-dot problem, where one of the two point masses is extruded into a line segment mass, thereby enabling it to spin. In this paper we further extend the dot-dot problem by extruding *both* point masses into line segment masses, thereby enabling *both* masses to spin. Predicting the motion of the Fig. 1 trojan binary asteroids is an approximate but natural example of such a slash-slash (//) body problem. Our results suggest that typical solutions are a pleasing mix of order and chaos, as in Fig. 2.

The slash-slash system is an instructive prototype for the interplay between rotation and revolution, which characterize asteroids but not the interaction of idealized points. For simplicity we focus on the planar slash-slash body problem, where initial conditions are constrained so that all motion is in a plane. Its diverse dynamics include a strongly stable orbit, families of unstable periodic orbits, spin-stabilized nonchaotic orbits, and generic chaotic orbits. Exploiting the system's extra degree of freedom, we show how angular momentum can flow from rotation to revolution and back, increasing or decreasing the slashes' spins while decreasing or increasing their orbit. Such angular momentum exchange can even unbind

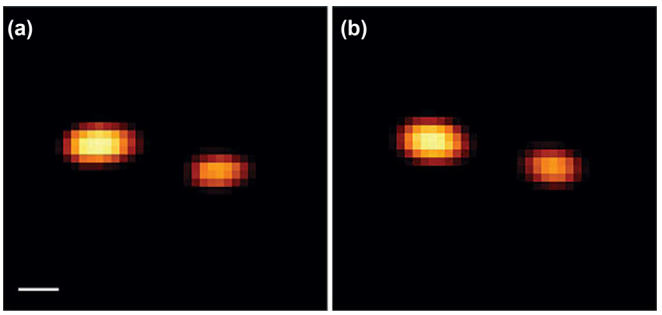

FIG. 1. (Color online) Trojan binary asteroid 617 Patroclus, infrared imaged at (a) 1.6 μm and (b) 2.2 μm, is an approximate slash-slash body system. Angular scale bar represents 50 mas and the components are separated here by 640 km. Reprinted by permission from Macmillan Publishers Ltd. [13], copyright 2006.

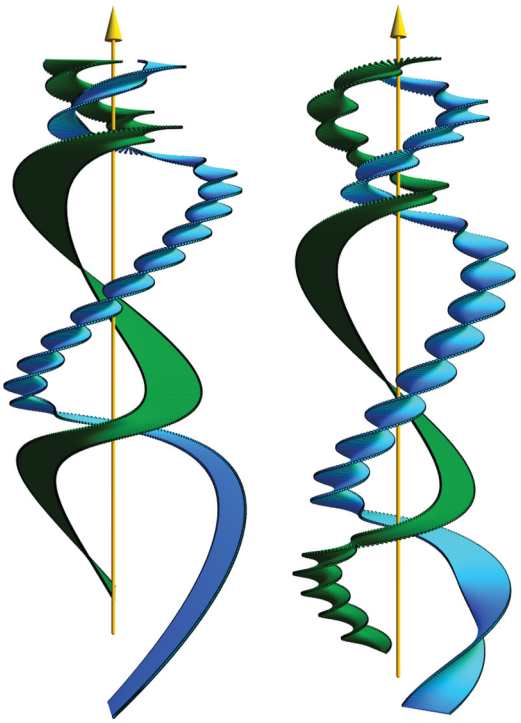

FIG. 2. (Color online) Typical spacetime plots of the rotation and revolution of two line segments or slashes demonstrating complex spin and orbital angular momentum exchanges. Arrows indicates time increasing upward.

the slashes in situations where two dots would remain bound, and this may have implications for asteroid rotation and escape rates [17,18]. In addition, retrograde motions where the slashes spin opposite to their orbits are stable, with regular dynamics and smooth initial condition spaces, while prograde motions are unstable, with chaotic dynamics and fractal initial condition spaces.

Section II below writes the gravitational potential energy of the slashes as a double integral over their lengths and explicitly evaluates the integral in closed form. It then uses the slash-slash Lagrangian to write the exact equations of motion. Finally, it expresses the forces and torques compactly in terms of vectors joining the ends and midpoints of the slashes and verifies the correct limiting behaviors. Section III discusses three exact solutions for special circular orbits. Section IV describes our techniques for numerically integrating the exact but nonlinear equations of motion and discusses some interesting orbits. Sections V and VI describe parameter space scans of the slashes' alignment and the product of their spins to probe the generic structure of the orbits. Section VII summarizes our results. The mathematics in this paper is explicitly checked by computer algebra [19].

II. THEORY

A. Potential energy

The Newtonian gravitational potential energy of two line segments or "slashes" of masses m_i, lengths $\ell_i = |\vec{\ell}_i|$, orientations $\hat{\ell}_i = \vec{\ell}_i/\ell_i$, and center-to-center separation $\vec{r} = r\hat{r}$ is

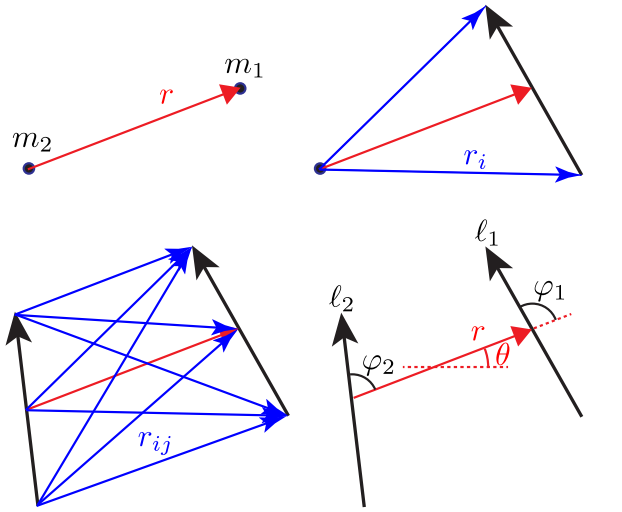

FIG. 3. (Color online) Geometry for the dot-dot, slash-dot, and slash-slash problems. The displacement $\vec{r}$ separates mass m_1 from mass m_2. Displacements $\vec{r}_{ij}$ separate the midpoint and ends of the two slashes. Vectors $\vec{\ell}_1$ and $\vec{\ell}_2$ encode the lengths and orientations of the slashes, which are at angles φ_1 and φ_2 from the displacement $\vec{r}$, which itself is at an angle θ from an inertial reference line.

$$V = \iint -G\frac{dm_1 dm_2}{r_{12}} = -G\frac{m_1 m_2}{\ell_1 \ell_2}\int_{-\ell_1/2}^{+\ell_1/2}\int_{-\ell_2/2}^{+\ell_2/2}\frac{d\lambda_1 d\lambda_2}{|\vec{r}+\lambda_1\hat{\ell}_1-\lambda_2\hat{\ell}_2|}. \quad (1)$$

Define the displacement vectors

$$\vec{r}_{ij} = \vec{r} + i\frac{\vec{\ell}_1}{2} - j\frac{\vec{\ell}_2}{2} \quad (2)$$

connecting the ends and centers of the slashes, as in Fig. 3, and denote the indices $i,j \in \{-1,0,+1\}$ by $\{n,o,p\}$. Evaluate the double integral explicitly [19] to find

$$V = -\frac{Gm_1m_2}{\ell_1\ell_2}\frac{\hat{\ell}_1\times\hat{\ell}_2}{|\hat{\ell}_1\times\hat{\ell}_2|^2}\cdot\left\{\hat{\ell}_1\times\left(\vec{r}_{op}\log\left[\frac{r_{np}+\vec{r}_{np}\cdot\hat{\ell}_1}{r_{pp}+\vec{r}_{pp}\cdot\hat{\ell}_1}\right]+\vec{r}_{on}\log\left[\frac{r_{pn}+\vec{r}_{pn}\cdot\hat{\ell}_1}{r_{nn}+\vec{r}_{nn}\cdot\hat{\ell}_1}\right]\right)+\hat{\ell}_2\times\left(\vec{r}_{po}\log\left[\frac{r_{pn}-\vec{r}_{pn}\cdot\hat{\ell}_2}{r_{pp}-\vec{r}_{pp}\cdot\hat{\ell}_2}\right]+\vec{r}_{no}\log\left[\frac{r_{np}-\vec{r}_{np}\cdot\hat{\ell}_2}{r_{nn}-\vec{r}_{nn}\cdot\hat{\ell}_2}\right]\right)\right\}. \quad (3)$$

If the slashes are short compared to their separation, $\ell_1,\ell_2 \ll r$, then

$$V \sim -\frac{Gm_1m_2}{r}\left[1+\frac{\ell_1^2(1+3\cos 2\varphi_1)+\ell_2^2(1+3\cos 2\varphi_2)}{48r^2}\right]. \quad (4)$$

The factors of 2 in the arguments of the cosines reflect the symmetry of the slashes. In terms of the o-plus and o-minus

logarithmic functions

$$\ominus^{ij}_{kl,m} = \log\left[\frac{r_{ij} \pm \vec{r}_{ij}\cdot\hat{\ell}_m}{r_{kl} \pm \vec{r}_{kl}\cdot\hat{\ell}_m}\right], \tag{5}$$

the potential energy is the sum of the box products

$$V = -\frac{Gm_1m_2}{\ell_1\ell_2}\frac{\hat{z}}{\sin\Delta}\cdot\big[\hat{\ell}_1\times\big(\ominus^{np}_{pp,1}\,\vec{r}_{op} + \ominus^{pn}_{nn,1}\,\vec{r}_{on}\big) + \hat{\ell}_2\times\big(\ominus^{pn}_{pp,2}\,\vec{r}_{po} + \ominus^{np}_{nn,2}\,\vec{r}_{no}\big)\big], \tag{6}$$

where $\hat{\ell}_1\times\hat{\ell}_2 = \hat{z}\sin\Delta$ and $\Delta = \varphi_2 - \varphi_1$ is the angle between the slashes. This expression is exact for all slash lengths; check it by shrinking the lengths to zero. If the length of one slash shrinks to zero, $V = V_{//}$ reduces to the slash-dot potential energy

$$V_{/\cdot} = -\frac{Gm_1m_2}{\ell}\log\left[\frac{r_p - \vec{r}_p\cdot\hat{\ell}}{r_n - \vec{r}_n\cdot\hat{\ell}}\right], \tag{7}$$

and if the length of the remaining slash shrinks to zero, $V_{/\cdot}$ in turn reduces to the familiar dot-dot potential energy

$$V_{\cdot\cdot} = -\frac{Gm_1m_2}{r}. \tag{8}$$

B. Lagrangian

Relative to the inertial center-of-mass, the kinetic energy

$$T = \tfrac{1}{2}m_1\dot{\vec{r}}_1\cdot\dot{\vec{r}}_1 + \tfrac{1}{2}m_2\dot{\vec{r}}_2\cdot\dot{\vec{r}}_2 + \tfrac{1}{2}I_1\dot{\phi}_1^2 + \tfrac{1}{2}I_2\dot{\phi}_2^2, \tag{9}$$

where the angles $\phi_i = \theta + \varphi_i$ and the rotational inertias $I_i = m_i\ell_i^2/12$. Alternately, write

$$T = \tfrac{1}{2}\mu(\dot{r}^2 + r^2\dot{\theta}^2) + \tfrac{1}{2}I_1(\dot{\theta}+\dot{\varphi}_1)^2 + \tfrac{1}{2}I_2(\dot{\theta}+\dot{\varphi}_2)^2, \tag{10}$$

where the reduced mass $\mu = m_1m_2/(m_1+m_2)$ and the relative displacement $\vec{r} = +m_1\vec{r}_1/\mu = -m_2\vec{r}_2/\mu$. Given the Lagrangian $L = T - V$, rearrange the Euler-Lagrange equations

$$\mu\ddot{r} = \frac{d}{dt}\frac{\partial L}{\partial\dot{r}} = \frac{\partial L}{\partial r} = -\frac{\partial V}{\partial r} + \mu r\dot{\theta}^2, \tag{11a}$$

$$\mu(r^2\ddot{\theta} + 2r\dot{r}\dot{\theta}) + I_1(\ddot{\theta}+\ddot{\varphi}_1) + I_2(\ddot{\theta}+\ddot{\varphi}_2) = \frac{d}{dt}\frac{\partial L}{\partial\dot{\theta}} = \frac{\partial L}{\partial\theta} = 0, \tag{11b}$$

$$I_1(\ddot{\theta}+\ddot{\varphi}_1) = \frac{d}{dt}\frac{\partial L}{\partial\dot{\varphi}_1} = \frac{\partial L}{\partial\varphi_1} = -\frac{\partial V}{\partial\varphi_1}, \tag{11c}$$

$$I_2(\ddot{\theta}+\ddot{\varphi}_2) = \frac{d}{dt}\frac{\partial L}{\partial\dot{\varphi}_2} = \frac{\partial L}{\partial\varphi_2} = -\frac{\partial V}{\partial\varphi_2}, \tag{11d}$$

for Newtonian analysis as

$$F_r = \mu(\ddot{r} - r\dot{\theta}^2) = -\frac{\partial V}{\partial r}, \tag{12a}$$

$$F_\theta = \mu(r\ddot{\theta} + 2\dot{r}\dot{\theta}) = \frac{1}{r}\left(\frac{\partial V}{\partial\varphi_1} + \frac{\partial V}{\partial\varphi_2}\right), \tag{12b}$$

$$\tau_{1z} = I_1(\ddot{\theta}+\ddot{\varphi}_1) = -\frac{\partial V}{\partial\varphi_1}, \tag{12c}$$

$$\tau_{2z} = I_2(\ddot{\theta}+\ddot{\varphi}_2) = -\frac{\partial V}{\partial\varphi_2}, \tag{12d}$$

and for numerical analysis as

$$\ddot{r} = -\frac{1}{\mu}\frac{\partial V}{\partial r} + r\dot{\theta}^2, \tag{13a}$$

$$\ddot{\theta} = +\frac{1}{\mu r^2}\left(\frac{\partial V}{\partial\varphi_1} + \frac{\partial V}{\partial\varphi_2}\right) - \frac{2\dot{r}\dot{\theta}}{r}, \tag{13b}$$

$$\ddot{\varphi}_1 = -\frac{1}{\mu r^2}\left(\frac{\partial V}{\partial\varphi_1} + \frac{\partial V}{\partial\varphi_2}\right) + \frac{2\dot{r}\dot{\theta}}{r} - \frac{1}{I_1}\frac{\partial V}{\partial\varphi_1}, \tag{13c}$$

$$\ddot{\varphi}_2 = -\frac{1}{\mu r^2}\left(\frac{\partial V}{\partial\varphi_1} + \frac{\partial V}{\partial\varphi_2}\right) + \frac{2\dot{r}\dot{\theta}}{r} - \frac{1}{I_2}\frac{\partial V}{\partial\varphi_2}. \tag{13d}$$

C. Force and torque

From Eq. (12) the radial component of the force between the slashes is the box product

$$F_r = -\frac{Gm_1m_2}{\ell_1\ell_2}\frac{\hat{z}}{\sin\Delta}\cdot\hat{r} \times\big[\hat{\ell}_1\big(\ominus^{np}_{pp,1} + \ominus^{pn}_{nn,1}\big) + \hat{\ell}_2\big(\ominus^{np}_{nn,2} + \ominus^{pn}_{pp,2}\big)\big]. \tag{14}$$

If the slashes are short compared to their separation, $\ell_1,\ell_2 \ll r$, then

$$F_r \sim -\frac{Gm_1m_2}{r^2}\left[1 + \frac{\ell_1^2(1+3\cos2\varphi_1) + \ell_2^2(1+3\cos2\varphi_2)}{16r^2}\right]. \tag{15}$$

Again the factors of 2 in the arguments of the cosine reflects the symmetry of the slashes. The azimuthal component of the force is the box product

$$F_\theta = -\frac{Gm_1m_2}{\ell_1\ell_2}\frac{\hat{z}}{\sin^2\Delta}\cdot\hat{r} \times\big\{\hat{\ell}_1\big[\ominus^{np}_{nn,2} + \ominus^{pn}_{pp,2} + \hat{\ell}_1\cdot\hat{\ell}_2\big(\ominus^{np}_{nn,1} + \ominus^{pn}_{pp,1}\big)\big] + \hat{\ell}_2\big[\ominus^{np}_{nn,1} + \ominus^{pn}_{pp,1} + \hat{\ell}_1\cdot\hat{\ell}_2\big(\ominus^{np}_{nn,2} + \ominus^{pn}_{pp,2}\big)\big]\big\}. \tag{16}$$

If the length of one slash shrinks to zero, the force reduces to the slash-dot force

$$\vec{F}_{/\cdot} = -\frac{Gm_1m_2}{\ell r}(\hat{r}_p - \hat{r}_n)\times\frac{\hat{\ell}\times\hat{r}}{|\hat{\ell}\times\hat{r}|^2} = -\frac{Gm_1m_2}{\ell r}\frac{\hat{z}\times(\hat{r}_p - \hat{r}_n)}{\sin\Delta}, \tag{17}$$

and if the length of the remaining slash shrinks to zero, $F_{/\cdot}$ in turn reduces to the famous dot-dot force

$$\vec{F}_{\cdot\cdot} = -\frac{Gm_1m_2}{r^2}\hat{r}. \tag{18}$$

The torque on slash 1 about its center

$$\tau_{1z} = \frac{Gm_1m_2}{\ell_1\ell_2}\left\{\big[\ominus^{np}_{nn,1} + \ominus^{pn}_{pp,1} + \hat{\ell}_1\cdot\hat{\ell}_2\big(\ominus^{np}_{pp,2} + \ominus^{pn}_{nn,2}\big)\big]\frac{r\sin\varphi_2}{\sin^2\Delta} - \frac{r_{nn} + r_{pp} - r_{pn} - r_{np}}{\sin\Delta}\right\}, \tag{19}$$

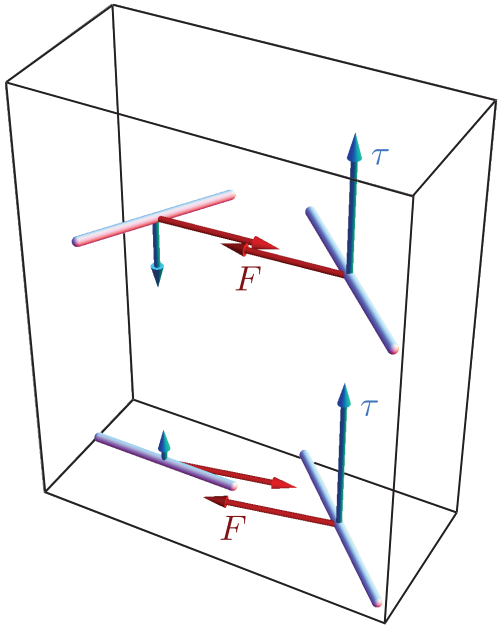

FIG. 4. (Color online) Forces $\vec{F}_i$ are equal and opposite but not necessarily along the line joining the slash centers. Torques $\vec{\tau}_i$ with respect to the slash centers need be neither equal nor opposite.

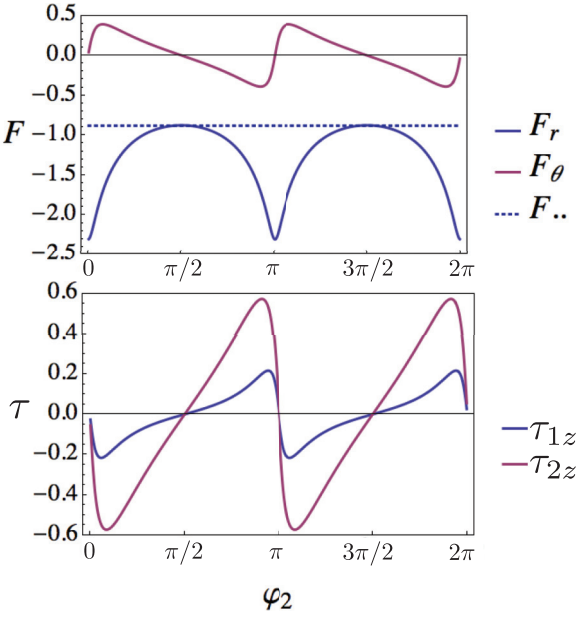

FIG. 5. (Color online) Torques τ_{1z} and τ_{2z} on both slashes and forces components F_r and F_θ on one slash as the other rotates through $0 \leqslant \varphi_2 \leqslant 2\pi$ corresponding to the bottom case of Fig. 4. The dotted line indicates the (radial) force $F_{..}$ if both slashes were dots.

and the torque on slash 2 about its center

$$\tau_{2z} = \frac{Gm_1m_2}{\ell_1\ell_2}\Big\{\big[\ominus^{np}_{nn,2} + \ominus^{pn}_{pp,2} + \hat{\ell}_1\cdot\hat{\ell}_2\big(\oplus^{np}_{pp,1} + \oplus^{pn}_{nn,1}\big)\big]\frac{r\sin\varphi_1}{\sin^2\Delta} + \frac{r_{nn}+r_{pp}-r_{pn}-r_{np}}{\sin\Delta}\Big\}, \tag{20}$$

where $\hat{r}\times\hat{\ell}_i = \hat{z}\sin\varphi_i$ defines the angles between the slashes and the line joining their centers. These torques need be neither equal nor opposite, as in Fig. 4, although the torque on the entire system about its center of mass always vanishes. As one slash rotates through 360° the force and torque on the other repeats twice, as in Fig. 5, due to the symmetry of the slashes. If the length of one slash shrinks to zero, the torques reduce to the slash-dot torque

$$\vec{\tau}_{/.} = -\frac{Gm_1m_2}{\ell}(\hat{r}_p-\hat{r}_n)\cdot\hat{r}\,\frac{\hat{\ell}\times\hat{r}}{|\hat{\ell}\times\hat{r}|^2} = \frac{Gm_1m_2}{\ell}\frac{(\hat{r}_p-\hat{r}_n)\cdot\hat{r}}{\sin\Delta}\hat{z}, \tag{21}$$

and if the length of the remaining slash shrinks to zero, the torques vanish, as they should for the dot-dot torque

$$\vec{\tau}_{..} = 0. \tag{22}$$

III. EXACT SOLUTIONS

Although a generic slash-slash orbit is chaotic, we were able to solve exactly for three kinds of circular orbits. If the slashes' separation r is constant, then Eq. (13a) reduces to

$$\omega = \dot{\theta} = \sqrt{\frac{1}{\mu r}\frac{\partial V}{\partial r}} = \sqrt{\frac{-F_r}{m_2 r_2}}. \tag{23}$$

We evaluated this expression [19] for three different scenarios: the "pointing" orbit $--$, where each slash lies along the line joining them; the "perpendicular" orbit $-|$, where one slash lines along the line joining them and the other is perpendicular to the line; and the "parallel" orbit $||$, where both slashes are perpendicular to the line joining them (but parallel to each other). By Eq. (23) the orbital frequencies and angular velocities of these circular orbits are

$$\omega_{--} = \omega_K\sqrt{\frac{r^2}{\ell_1\ell_2}\log\left[\frac{4r^2-(\ell_1-\ell_2)^2}{4r^2-(\ell_1+\ell_2)^2}\right]}, \tag{24a}$$

$$\omega_{-|} = \omega_K\sqrt{\frac{r^2}{\ell_1\ell_2}\log\left\{\frac{\big[\sqrt{\ell_2^2+(\ell_1-2r)^2}+\ell_2\big]\big[\sqrt{\ell_2^2+(\ell_1+2r)^2}-\ell_2\big]}{\big[\sqrt{\ell_2^2+(\ell_1-2r)^2}-\ell_2\big]\big[\sqrt{\ell_2^2+(\ell_1+2r)^2}+\ell_2\big]}\right\}}, \tag{24b}$$

$$\omega_{||} = \omega_K\sqrt{\tfrac{r}{\ell_1\ell_2}\big[\sqrt{4r^2+(\ell_1+\ell_2)^2}-\sqrt{4r^2+(\ell_1-\ell_2)^2}\big]}, \tag{24c}$$

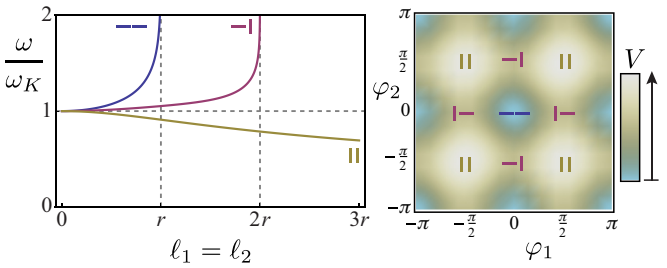

FIG. 6. (Color online) Orbital frequencies ω normalized to the Kepler frequency ω_K versus a common slash length $\ell_1 = \ell_2$ for the pointing, perpendicular, and parallel configurations (left), where vertical asymptotes correspond to slash intersections. Special orbits occupy potential energy V versus initial angles φ_1 and φ_2 extrema (right).

where from Kepler's third law $\omega_K = \sqrt{G(m_1 + m_2)/r^3}$ is the orbital frequency of two dots.

All three circular frequencies correctly reduce to the two corresponding slash-dot body circular frequencies when the length of one of the slashes shrinks to zero [16]. The frequencies obey $\omega_{--} \geqslant \omega_{-|} \geqslant \omega_K \geqslant \omega_{||}$, as in Fig. 6. Heuristically, if two dots are extruded to slashes parallel to the line joining them, the mean gravitational force (and hence the orbital frequency) increases because of the nonlinear inverse-distance-squared nature of the force. The same effect is present but lesser if one slash is extruded perpendicular to the line joining them, and the opposite effect is obtained if both slashes are extruded perpendicular to the line joining them. The forces (and hence the frequencies) diverge if two slashes touch. The Fig. 6 potential energy as a function of initial angles suggests, and numerical integration confirms, that the pointing orbit is stable but the perpendicular and parallel orbits are not.

IV. NUMERICAL INTEGRATION

The Sec. II exact equations of motion greatly expedite numerical integration of slash-slash orbits. However, the force and torque expressions suffer a $0/0$ instability when the slashes are parallel. This occurs, for example, when the relative angle between the slashes $\Delta = 0$ in the Eq. (17) force law. One basic approach to resolving this issue is to multiply the numerator and denominator by a large constant, when the denominator is near zero, to keep more significant digits in the computed quotient. Another option is to add a very small constant to the formula's denominator [20], so that a $0/0$ case yields a zero quotient, while the quotient is largely unchanged in other situations. If the exact value at the singularity can be computed via L'Hôpital's rule, then it can be applied whenever the numerator and denominator are both sufficiently near zero. We chose the last of these approaches, along with using high working precision, which reduces the size of the neighborhood on which the exact solution at the singularity must be applied.

In Obj-C/C++ we coded an adaptive step size Runge-Kutta-Fehlberg (RKF) algorithm [21,22] to integrate the equations of motion. A standard method for solving nonstiff differential equations, the RKF algorithm computes both fourth-order and fifth-order Runge-Kutta approximations at each step, using the latter to estimate the error associated with the former. Given a specified error tolerance, which we fixed at 5×10^{-5} by balancing computation time versus integration accuracy, the error estimate determines the appropriate size of the next step, as well as when a step should be repeated. By careful selection of the function evaluation points and their weights, this algorithm requires only six function evaluations per step, as compared to ten with a less-sophisticated approach. By using very small step sizes only when necessary, the RKF method requires far fewer steps than the classic RK4 method, to obtain a given level of accuracy. Using RKF, we integrated the equations of motion in 64 digit precision using the GNU multiple precision arithmetic floating point libraries GMP [23] and MPFR [24]. We deployed this program concurrently on multiple processors for two-dimensional parameter space scans and checked our accuracy by monitoring the relative change in the system's total energy and angular momentum. We further cross checked the orbits using *Mathematica* [25] at large working precision.

Figure 7 summarizes a typical evolution, where the relative numerical change in energy and angular momentum

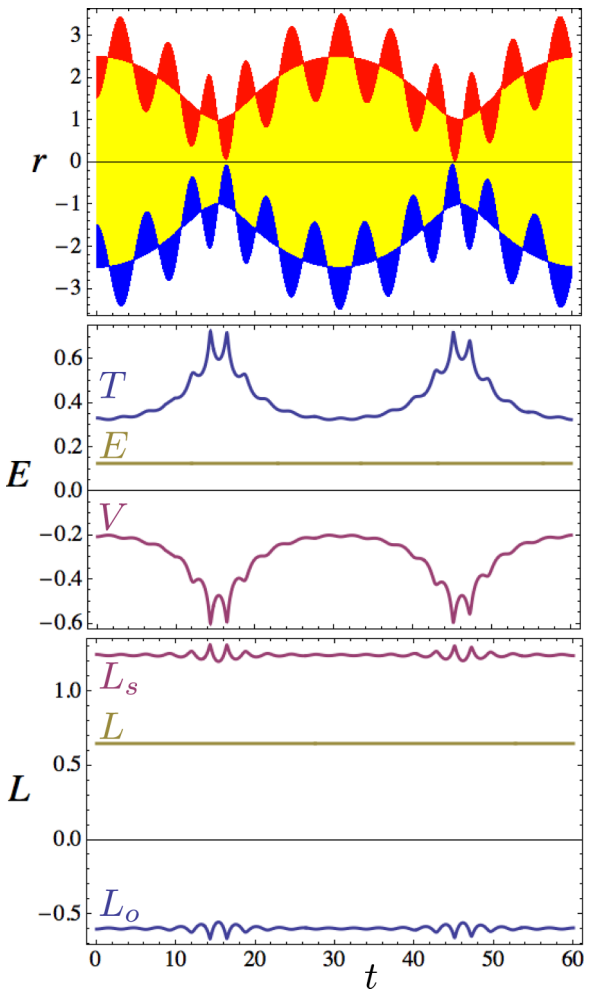

FIG. 7. (Color online) Example time series. Top: Red (light gray) and blue (dark gray) projections of the slashes on the line $\vec{r}$ joining their centers. Middle: Conserved energy E shuffling between kinetic T and potential V. Bottom: Conserved angular momentum L shuffling between spin L_S and orbit L_O.

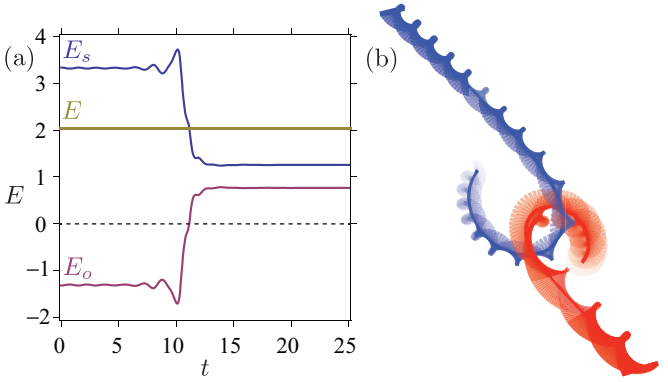

FIG. 8. (Color online) Escape from the slash-slash body system. (a) In a time series plot, initially the orbit energy $E_O = E - E_S$ is negative indicating a bound orbit for the corresponding dot-dot system, but (b) in a strobed animation, a close encounter transfers energy from spin E_S to orbit E_O unbinding the slash-slash system.

are $\delta E/E \sim 10^{-6}$ and $\delta L/L \sim 10^{-7}$. The top graph plots $(\mu r/m_1 + \ell_1 \cos\varphi_1)/2$ and $(-\mu r m_2 + \ell_2 \cos\varphi_2)/2$ as a function of time to suggest the dynamic interplay between rotation and revolution. The bottom graphs illustrate the interplay between kinetic and potential energy and spin and orbital angular momentum.

Figure 8 demonstrates a dramatic escape. The orbital energy of the slash-slash system is negative, so the corresponding dot-dot system would be permanently bound. However, energy stored in the slashes' spins makes the system energy positive, indicating the possibility of escape. Indeed, a close encounter, illustrated by the strobed animation, transfers energy from spin to orbit liberating the slashes.

Such encounters suggest one mechanism by which asteroids or meteoroids escape from belt or ring systems. The inverse process, where energy flows from orbit to spin, suggest one reason why some asteroids have anomalously high spins.

V. ALIGNMENT SPACE

To systematically sample a broad range of slash-slash orbits, we numerically integrated the exact but nonlinear Eq. (13) equations of motion over a wide range of initial conditions and parameters. Each point in a two-dimensional plot corresponded to a different orbit and was colored (shaded) according to some measure of the outcome.

For example, to study the relationship between the slashes' spins, we defined the alignment

$$\mathcal{A} = \mathcal{A}_{12} = \hat{\ell}_1 \cdot \hat{\ell}_2 = \cos\Delta = \cos[\varphi_2 - \varphi_1] \qquad (25)$$

as a natural extension of the alignment defined in the study of the slash-dot body problem [16]. The alignment $\mathcal{A} = \pm 1$ when the slashes are parallel, and the alignment $\mathcal{A} = 0$ when the slashes are perpendicular.

Figure 9 plots the alignment $\mathcal{A}$ in a red-white-blue (grayscale) palette as a function of the initial orbital angular velocity ω, initial slash spin angular velocity ω_1, and slash length ℓ_1 (with fixed slash length ℓ_2), after one revolution $\theta = 2\pi$, for pointing initial conditions. Black codes collisions, or near collisions, as in practice we abort the simulations just

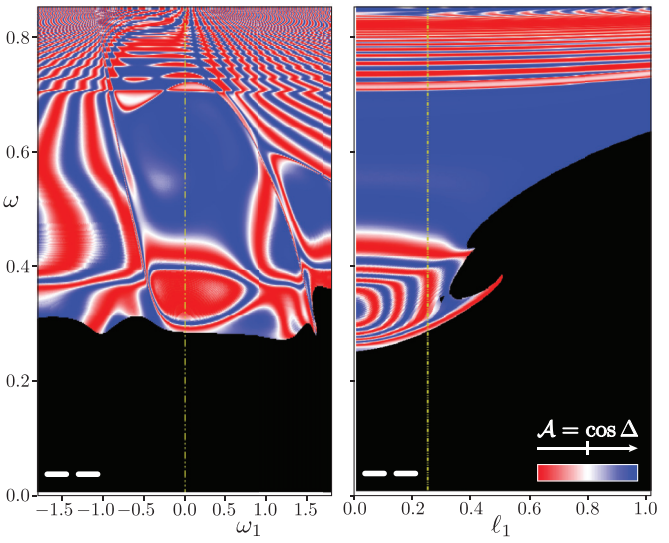

FIG. 9. (Color online) Colors (shades) code the alignment $\mathcal{A}$ versus initial orbital angular velocity $\omega = \dot{\theta}_0$ and initial spin angular velocity ω_1 (left) and $\mathcal{A}$ versus ω and slash length ℓ_1 (right), with blue (dark gray) positive, red (light gray) negative, white zero, and black collision, after one revolution $\theta = 2\pi$, for pointing initial conditions. Vertical dot-dash lines indicate the intersection of the two plots.

before contact to prevent our adaptive step size integrator from wasting time. The dot-dash lines indicate the intersection of these cross-sectional plots.

Reminiscent of similar plots for the slash-dot system, low orbital velocities and long slash lengths imply collisions. Striped patterns correspond to sequences of unstable periodic orbits. The stable pointing orbit dominates the broad central alignment region.

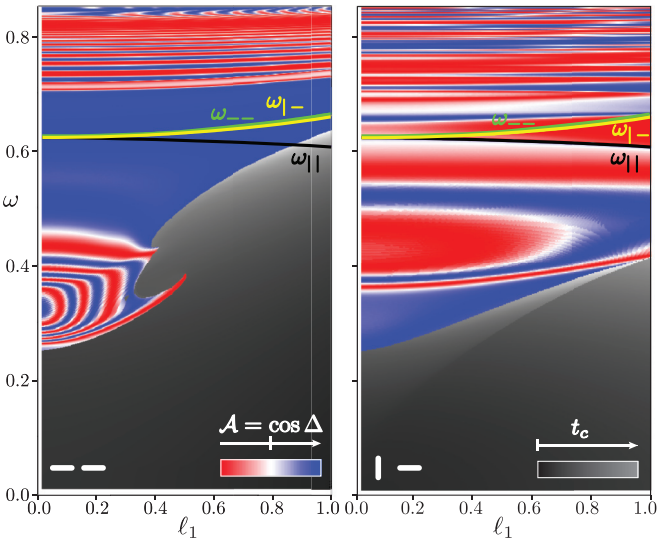

FIG. 10. (Color online) Colors (shades) code the alignment $\mathcal{A}$ versus initial orbital angular velocity $\omega = \dot{\theta}_0$ and slash length ℓ_1, with blue (dark gray) positive, red (light gray) negative, white zero, and intermediate grays collision time t_c, after one revolution $\theta = 2\pi$, for pointing (left) and perpendicular (right) initial conditions. Superimposed are ω_{--}, $\omega_{-|}$, and $\omega_{||}$ as a function of ℓ_1.

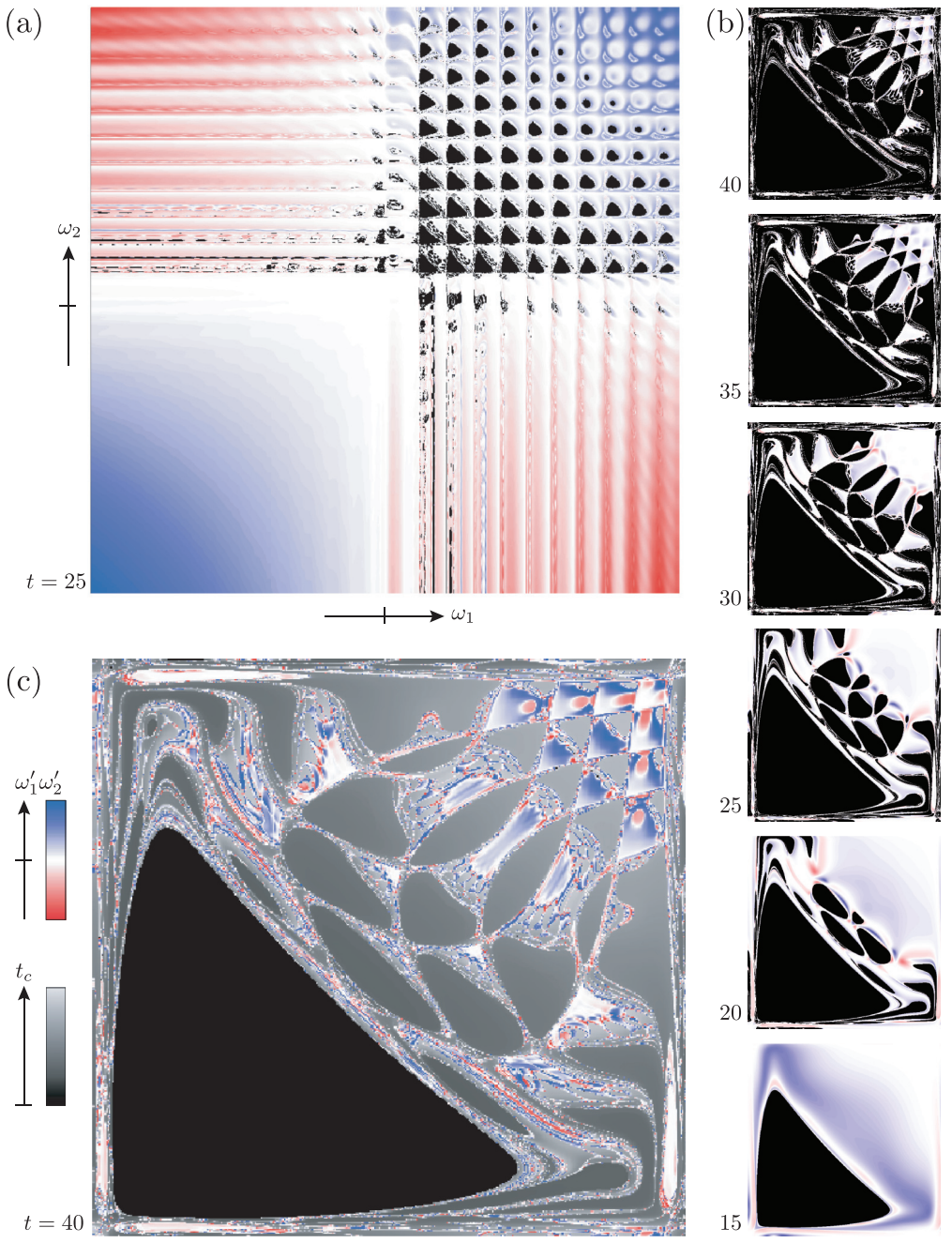

FIG. 11. (Color) For asymmetric start $\varphi_1 \neq \varphi_2$, (a) colors code final spin products $\omega_1'\omega_2'$ as a function of the initial spins ω_1 and ω_2, (b) magnified time sequence, and (c) further magnification, where grays codes collision times t_c.

Figure 10 plots the alignment $\mathcal{A}$ as a function of the initial orbital angular velocity ω and slash length ℓ_1, after one revolution $\theta = 2\pi$, for both pointing and perpendicular initial conditions. Intermediate grays code time to collision. Superimposed are the Eq. (24) exact circular angular velocities. The stable ω_{--} dominates the alignment plot for pointing initial conditions, but the unstable $\omega_{|-}$ does *not* dominates the alignment plot for perpendicular initial conditions, as expected.

VI. SPIN PRODUCT SPACE

To further investigate the relationship between spin and orbit in the slash-slash body problem, we plotted the product of the slashes' spins $\omega_1'\omega_2'$ after a fixed time t versus their initial spins ω_1 and ω_2 in a red-white-blue palette where black again denotes collisions. Figure 11 summarizes the situation for asymmetric starts, in which the slashes begin pointing in different directions.

The top-left plot has four well-defined quadrants $\{\pm,\pm\}$. When both spins are negative $\{-,-\}$, and hence "against the orbit" or retrograde, the orbits are stable in that small changes in initial condition do not significantly change the final conditions, corresponding to continuous color changes. However, when both spins are positive $\{+,+\}$, and hence "with the orbit" or prograde, the orbits are unstable in that small changes in the initial condition can dramatically change the

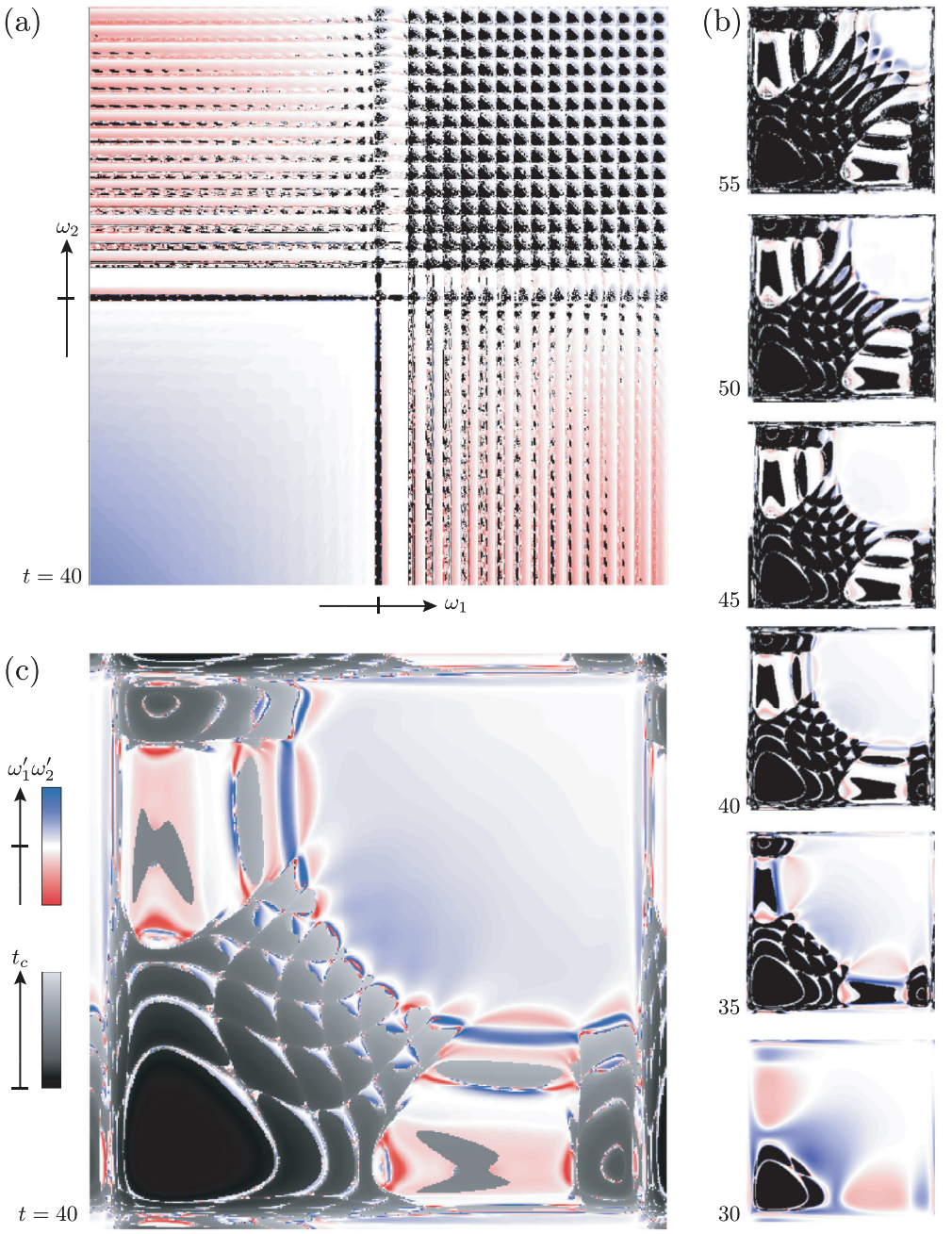

FIG. 12. (Color) For symmetric start $\varphi_1 = \varphi_2$, (a) colors code final spin products $\omega_1'\omega_2'$ as a function of the initial spins ω_1 and ω_2, (b) magnified time sequence, and (c) further magnification, where grays codes collision times t_c.

final condition, corresponding to discontinuous color changes. When the spins are mixed $\{+,-\}$ or $\{-,+\}$, the orbits are stable in the direction of the negative spin and unstable in the direction of the positive spin. In a reference frame rotating with the mean orbital angular velocity, the retrograde spins are fastest and most stable.

The cell structure in the $\{+,+\}$ quadrant corresponds to orbits differing by an integer number of spin flips. Moving vertically, by fixing ω_1 and increasing ω_2, each successive cell starts an orbit with an extra 180° half flip of slash 2, at least for short times. Similarly, moving horizontally, by fixing ω_2 and increasing ω_1, each successive cell starts an orbit with an extra 180° half flip of slash 1.

The right-side sequence illustrates the time development of these structures. The black collision region expands hinting at a fractal web of noncollisional orbits all related by patterns of extra spin flips. The bottom-right plot is a closeup of this cell structure, where now grays code collision times.

The intricate, fractal-like structure inside the individual cells is interesting as well. Moving along a 45° line from triangle to triangle in the top-right corner of an individual cell, one slash gains a half flip and the other loses a half flip per orbit, again at least for short times.

Figure 12 summarizes the spin products for symmetric starts, in which the slashes begin pointing in the same direction. In this case, the spin product space is symmetric about the main

diagonal $\omega_1 = \omega_2$, as expected. The magnified time sequence and the $t = 40$ magnification use slightly different definitions of "near collision" to abort the integrations; typical minimum distances were 0.05 and 0.025.

VII. CONCLUSIONS

The slash-slash body problem is of theoretical, numerical, and practical interest. It extends a classical problem in mathematical physics and yields rich results and important insights. For example, the force between the slashes is equal (in magnitude) and opposite (in direction), but not along the line joining the centers of the slashes, and the torques on the slashes are typically neither equal nor opposite. Furthermore, retrograde spins are stable while prograde spins are unstable. Such results help break bad habits and build good intuition for the full body problem, which becomes more important as deep space flight activity increases. Indeed, the slash-slash problem and its solution may elucidate the dynamics of asteroids and large space structures, both of which are relevant to NASA's current plan to send astronauts to rendezvous with a small asteroid captured into a lunar orbit.

Future work includes quantifying the chaos in the slash-slash body problem. For example, numerically estimating the maximum Lyapunov exponent as a function of pairs of parameters, like slash length and initial orbital angular velocity, would nicely complement the alignment plots of Figs. 9 and 10. We anticipate that the blue (dark gray) aligned regions would exhibit negative maximum Lyapunov exponents, reflecting the stability of the pointing orbit, while the misaligned (striped) regions would exhibit positive maximum Lyapunov exponents, which are hallmarks of chaos. We also hope to extend the slash-slash body problem from two to three dimensions. Among other phenomena, we expect to observe the rotation of the orbital plane due to the transfer of angular momentum from spin to orbit, perhaps both rhythmically and chaotically, for at least some parameters and initial conditions.

[1] S. Chandrasekhar, *Newton's Principia for the Common Reader* (Clarendon, Oxford, 1995), Secs. 1 and 15.

[2] V. G. Szebehely and H. Mark, *Adventures in Celestial Mechanics* (Wiley, New York, 1998).

[3] H. Poincaré, *New Methods of Celestial Mechanics* (American Institute of Physics, New York, 1993); *Les Méthodes Nouvelles de la Mécanique Céleste* (Gauthier-Villars, Paris, 1892, 1893, 1899).

[4] M. C. Gutzwiller, Rev. Mod. Phys. **70**, 589 (1998).

[5] C. Marchal, *Three-Body Problem* (Elsevier, Amsterdam, 1990).

[6] M. Valtonen and H. Karttunen, *The Three-Body Problem* (Cambridge University Press, Cambridge, 2006).

[7] J. F. Lindner, M. I. Roseberry, D. E. Shai, N. J. Harmon, and K. D. Olaksen, Int. J. Bifurcat. Chaos **18**, 455 (2008).

[8] J. C. Sprott, Am. J. Phys. **77**, 783 (2009).

[9] T. Lee, M. Leok, and N. H. McClamroch, Celestial Mech. Dyn. Astr. **98**, 121 (2007).

[10] A. Celletti and V. Sidorenko, Celestial Mech. Dyn. Astr. **101**, 105 (2008).

[11] V. Sidorenko and A. Celletti, Celestial Mech. Dyn. Astr. **107**, 209 (2010).

[12] B. Escribano, J. Vanyo, I. Tuval, J. H. E. Cartwright, D. L. González, O. Piro, and T. Tél, Phys. Rev. E **78**, 036216 (2008).

[13] F. Marchis *et al.*, Nature (London) **439**, 565 (2006).

[14] M. T. Zuber *et al.*, Science **289**, 2097 (2008).

[15] A. Elipe and M. Lara, J. Astronaut. Sci., **51**, 391 (2003).

[16] J. F. Lindner, J. Lynn, F. W. King, and A. Logue, Phys. Rev. E **81**, 036208 (2010).

[17] S. G. Love and T. J. Ahrens, Nature (London) **386**, 154 (1997).

[18] C. Jaffé, S. D. Ross, M. W. Lo, J. Marsden, D. Farrelly, and T. Uzer, Phys. Rev. Lett. **89**, 011101 (2002).

[19] See Supplemental Material at http://link.aps.org/supplemental/10.1103/PhysRevE.89.042917 for a *Mathematica* notebook that checks all the major calculations in this article.

[20] W. H. Press, S. A. Teukolsky, W. T. Vetterling, and B. P. Flannery, *Numerical Recipes in C: The Art of Scientific Computing* (Cambridge University Press, Cambridge, 1992).

[21] R. L. Burden and J. D. Faires, *Numerical Analysis* (Thomson Brooks/Cole, Belmont, 2005).

[22] E. Fehlberg, Computing **6**, 61 (1970).

[23] GMP Multiple Precision Arithmetic Library at gmplib.org (2012).

[24] MPRF Multiple Precision Floating point arithmetic library with correct Rounding at www.mpfr.org (2012).

[25] Wolfram Research, Inc., *Mathematica, Version 9.0* (Champaign, Illinois, 2013).